



Constitutive model for nickel alloy 690 (*Inconel 690*) at various strain rates and temperatures



Jérôme Blaizot ^{a, b}, Thibaut Chaise ^a, Daniel Nélías ^{a, *}, Michel Perez ^b,
Sophie Cazottes ^b, Philippe Chaudet ^a

^a Université de Lyon, INSA-Lyon, LaMCoS UMR CNRS 5259, F69621 Villeurbanne, France

^b Université de Lyon, INSA-Lyon, MATEIS UMR CNRS 5510, F69621 Villeurbanne, France

ARTICLE INFO

Article history:

Received 2 March 2015

Received in revised form 24 August 2015

Available online 17 October 2015

Keywords:

B. Elastic-viscoplastic material

B. Constitutive behaviour

A. Thermomechanical processes

A. Microstructures

A. Strengthening mechanisms

ABSTRACT

Mechanical behavior of nickel alloy 690 (NY690) is characterized from 25 °C to 1100 °C and for a strain rate ranging from 10^{-4} to $5 \times 10^{-3} \text{ s}^{-1}$. The effects of chromium carbides and grain size (50–150 μm) on the tensile properties of NY690, were studied at 25 °C and 750 °C. Chromium carbides have negligible influence on the yield stress and on the strain hardening whereas the grain size slightly decreases the yield stress and the hardening rate at room temperature. The grain size has little influence on the strain-hardening but increases the steady-state stress. The dislocation density is the major microstructural parameter governing the mechanical behavior of the alloy for the studied experimental conditions. The Kocks–Mecking–Estrin formalism is adapted to a wide range of temperature and strain rate to predict the mechanical behavior.

© 2015 Elsevier Ltd. All rights reserved.

1. Introduction

Ni-base super-alloys exhibit excellent corrosion resistance and high temperature mechanical properties (Reed, 2006), which makes them very good candidates for specific applications in a wide range of industries, including aerospace (e.g. turbine blade, turbine disc) and power generation (e.g. pressurized water reactor steam generator heat-transfer tubing), as mentioned by Harrod et al. (2001). Among all Ni-base alloys, Ni alloy 690, also called alloy 690 and further mentioned NY690, must satisfy the following requirements for pressurized water reactor components: resistance to stress corrosion cracking, manufacturability, weldability and availability (reasonable economics).

Welding is a critical fabrication technique for NY690 (DuPont et al., 2009), the challenge being to keep the corrosion resistance and mechanical properties of the welded joints. Welding is a very complex process during which the parts are simultaneously subjected to thermomechanical loading, as well as microstructural evolutions. In order to optimize the final properties of the assembly (particularly in terms of residual stress), one has to control and predict both thermomechanical response and microstructural evolutions of the Heat Affected Zone (HAZ). For that purpose engineers need an accurate constitutive law that (i) accounts for microstructural evolutions occurring during welding; (ii) can be used within the temperature range (from room temperature to melting temperature) and strain rate range (from 10^{-4} to $5 \times 10^{-3} \text{ s}^{-1}$) classically encountered during welding; (iii) can be easily implemented in a commercial Finite Element (FE) software.

* Corresponding author.

E-mail address: daniel.nelias@insa-lyon.fr (D. Nélías).

During the welding of NY690, several microstructural evolutions influencing mechanical properties may occur: grain growth, recrystallization, recovery and coarsening/dissolution of precipitates (Park et al., 2007).

Relationships between microstructure and mechanical properties of NY690 have been experimentally studied by Diano et al. (1989). Their study revealed that tensile properties are mainly controlled by the grain size and dislocation density whereas recrystallization and precipitation phenomenon rather playing an indirect role on the grain size.

Dynamic recrystallization may also occur in Ni-base alloys, as studied by Guo et al. (2011) and Wu et al. (2012) in the temperature range of 950–1200 °C. However, the high strain rate (0.03–3.3 s⁻¹) used by these authors clearly falls out of the domain concerned here, discarding thus dynamic recrystallization as a possible mechanism occurring during welding.

The precipitation of grain boundary carbides at high temperature is a common phenomenon in Ni-base alloys. For Ni alloy 600, the effect of intergranular carbides such as M₇C₃ on the tensile properties has been studied by Wang and Gan (2001). Their work shows a negligible effect of carbides on tensile properties.

The strain hardening behavior of NY690 has been studied by Venkatesh and Rack (1998). They showed different hardening regimes as a function of the temperature and modeled hardening behavior considering dislocation–dislocation interactions. Unfortunately, this study is limited to a single strain rate (10⁻³ s⁻¹), and more important is restricted to the prediction of the steady-state flow stress (neither yield stress nor hardening are simulated) considering only the dislocation density as a microstructural variable.

In terms of constitutive modeling, several approaches could be used. At the scale of a single crystal, crystal plasticity models can predict the hardening and texture heterogeneities as mentioned by Choi et al. (2013) and Jung et al. (2013). These models are particularly useful for understanding elementary plastic events and their connection with the macroscopic scale. However, these approaches hardly lead to fully consistent constitutive laws.

At the other end, phenomenological models developed by Chaboche (2008), Khan and Liu (2012) and more recently by Zhou et al. (2015) are extensively used since they can be easily implemented in FE software. However, they do not include microstructural parameters, limiting thus their validity to a given microstructure. Other phenomenological laws such as the one mentioned recently by Puchi-Cabrera et al. (2013) permit to account for temperature and strain rate effects, using the relationship provided by Sellars and McTegart (1966), which takes into account temperature and strain rate, but not the dislocation density. Recently, Galindo-Nava and Rivera-Díaz-del-Castillo (2013) presented a physically based thermo-statistical modeling of mechanical behavior, validated on various FCC metals. This modeling approach requires as input many physical parameters, not known for NY690, and cannot be easily implemented in FE softwares.

Dislocation-based models such as the Kocks–Mecking–Estrin (KME) model are used to determine the flow stress in a wide range of temperature. Following the pioneering contribution of Bergström (1970), Mecking and Kocks (1981) proposed a versatile and relatively simple framework, based on the evolution of the dislocation density. This approach was later improved by the same team (see Estrin and Mecking (1984), Estrin (1998, 2007) and Kocks and Mecking (2003)) and has then been adopted by many others such as Csanádi et al. (2014).

The effects of microstructure, such as precipitates and grain boundaries can be relatively straightforwardly included in the KME formalism, as mentioned by Estrin (1998) and Bardel et al. (2015). Note that to the authors' knowledge, the influence of microstructure such as grain size and precipitates on strain hardening of NY690 has not been studied yet.

The purpose of this study is to characterize NY690 in thermomechanical conditions representative of welding. A constitutive law will be proposed for temperatures ranging from 25 °C to 1000 °C, for strains up to 0.20 and strain rates ranging from 10⁻⁴ to 5 × 10⁻³ s⁻¹. The effects of grain size and precipitates will be discussed. After a description of experimental procedures and techniques (Section 2), microstructural and mechanical characterization will be presented in Section 3. A simple and versatile KME based constitutive model is proposed and parameterized in Section 4. The model validation for different experimental conditions is presented in Section 5. Hence the model and data presented here can be used for the simulation of fast thermo-mechanical treatments such as welding. Note that ductility may drastically change in the melted zone. However, this phenomenon falls out of the scope of this paper.

2. Materials and methods

2.1. Materials

NY690 was supplied in the form of a plate from Aubert & Duval with the chemical composition given in Table 1.

The as-received state permits to analyze the properties of the material in its original state before welding. As-received state was obtained through a 68 min annealing treatment at 1050 °C followed by a water quenching and a 5 h aging treatment at 725 °C followed by an air quenching. This aging at 725 °C is done to improve the ductility avoiding a cellular precipitation (Sabol and Stickler, 1969).

Table 1
Chemical composition of alloy NY690 from Aubert & Duval measurements.

	Ni	Cr	Fe	Mn	Si	Ti	Al	C
wt.%	60.3	29.2	10.1	0.32	0.28	0.24	0.13	0.018
at.%	57.1	31.5	10.2	0.33	0.27	0.28	0.27	0.084

2.2. Heat treatments

In order to quantify the effect of grain boundary carbides on the mechanical behavior, three microstructural states resulting from three different thermal treatments are studied (Table 2): as-received (AR), solid solution (SS) and fully precipitated (FP). These heat treatments start with a solution-annealing treatment at zero force using a thermo-mechanical testing machine Gleeble® 3500. The Gleeble® 3500 system permits to heat the tensile specimen by Joule's effect at a controlled heating rate under desired atmosphere and to perform quench in water or air. The Gleeble® 3500 mechanical system is a complete, fully integrated hydraulic servo system capable of doing tensile tests up to the melting temperature with high displacement rate.

The first step of the solution-annealing treatment is to heat from 25 °C to 1150 °C at a heating rate of 100 °C/s. Then, the tensile specimen is maintained for 1 h at 1150 °C under reduced pressure ($p = 30$ Pa) to avoid oxidation (Table 2). Finally, the solution-annealed specimen is water quenched at a cooling rate of about 500 °C/s. This heat treatment fully dissolves the grain boundary carbides and is referred as the solid solution state (SS) as mentioned by Kai et al. (1989) and Li et al. (2013).

The shortest incubation time for the carbide precipitation ranges between 800 °C and 900 °C (Wang and Gan, 2001). A fully precipitated state is consequently obtained through a treatment at 900 °C for 17 min followed by a water quenching. This heat treatment provides a continuous intergranular precipitation allowing the investigation of their role on mechanical properties. The resulting state is referred as fully precipitated state (Table 2). This will be further detailed in Section 3.1.

To study the effect of grain size on mechanical behavior, three solution-annealed heat treatments have also been performed (Table 3). Also, there is no interaction with chromium carbides that can modify the mechanical behavior.

Table 2

Heat treatments performed on the as-received (AR) state to quantify the effect of grain boundary carbides.

Microstructural state	Heat treatment
Solution annealed (SS-90 μm)	AR + 60 min at 1150 °C
Fully precipitated (FP)	AR + 60 min at 1150 °C + 17 min at 900 °C

Table 3

Heat treatments performed on the As-Received (AR) state to quantify the effect of grain size.

Microstructural state	Heat treatment
Solution annealed (SS-75 μm)	AR + 15 min at 1150 °C
Solution annealed (SS-90 μm)	AR + 60 min at 1150 °C
Solution annealed (SS-150 μm)	AR + 90 min at 1200 °C

2.3. Microstructural and mechanical characterization

2.3.1. Microstructural characterization

Optical microscopy was used to determine the grain size. Specimens were prepared by electro-etching at 25 °C during 15 s with 2.5 V direct current solution containing 25% HNO₃, 25% H₃PO₄ and 50% water (volume fraction) to reveal grain boundaries. The grain size distribution was determined from optical images by using the software *Image J*. Each optical image was firstly converted to a binary image, for which grain boundaries were manually drawn with a black line. Then, a threshold was selected so that only the grain boundaries appear on the picture. Grain area and number were automatically determined by the software *Image J*. The equivalent diameter was then calculated assuming a circular shape of the grains based on the grain area calculation by *Image J* for at least 1000 grains for each sample.

The location and morphology of precipitates was studied by Scanning Electron Microscopy (SEM). An electro-etching time of 10 s was used to reveal Cr₂₃C₆ precipitates. Precipitates were observed using a ZEISS Supra55 VP SEM operating at 10 kV and using Secondary Electron (SE) Imaging. The chemical composition of precipitates and dislocation structure were studied using Transmission Electron Microscopy (TEM). Samples are prepared by jet electro-polishing with 30 V direct current in a solution containing 20% HClO₄ and 80% C₂H₅OH (volume fraction) at -40 °C. Observations were made on a JEOL 2010 FEG TEM, equipped with an HAADF detector, and operating at 200 kV.

2.3.2. Uniaxial loadings

Cylindrical specimens of 6 mm in diameter and 40 mm in length were machined from as-received plate to perform isothermal tensile tests. Tensile tests were carried out on the Gleeble® 3500 mechanical system from 25 to 1000 °C with a

constant strain rate ranging from 10^{-4} to 10^{-1} s^{-1} . The tensile specimens were first heated at a rate of $25 \text{ }^\circ\text{C min}^{-1}$, maintained during 10 s and deformed up to a true strain of 0.20. During the tensile test, the strain and the strain-rate were controlled by a high-temperature extensometer HZT071 for which the gauge length is 10 mm and the temperature is almost constant ($\pm 5 \text{ }^\circ\text{C}$) in this zone. Above $750 \text{ }^\circ\text{C}$, cylindrical specimens of 10 mm in diameter and 140 mm in length were used leading to a constant temperature ($\pm 2 \text{ }^\circ\text{C}$) within the strain measurement zone. The true strain is calculated by using the displacement measured by the extensometer. Constant strain rate compression tests were also performed at room temperature in the strain rate range of 10^{-4} to 10^{-1} s^{-1} . Cylindrical specimens of 9 mm in diameter and 15 mm in height were machined from an as-received plate to perform compression tests.

3. Experimental results

3.1. Microstructural characterization

The microstructure of as-received NY690 is composed of equiaxed grains with a grain size ranging from 30 to $50 \text{ }\mu\text{m}$, few of them containing twins (Fig. 1). It contains large titanium nitrides ($0.1 - 1 \text{ }\mu\text{m}$) and intergranular carbides (Figs. 2 and 3) in the face-centered cubic (FCC) matrix. The crystallographic structure of the coherent M_{23}C_6 precipitates (FCC with a lattice parameter three times higher than the one of the matrix) was confirmed using diffraction pattern analysis (TEM), and EDX chemical measurement revealed that their composition is Cr_{23}C_6 (Fig. 3). Most of the carbides form discontinuous layers at grain boundaries, and some are located inside the grains with rather spherical shapes. In the as-received state, the dislocation density, measured from TEM images, is about $(3 \pm 2) \times 10^{13} \text{ m}^{-2}$. TEM micrographs (Fig. 4) indicate that groups of planar slip bands are lying on $\{111\}$ planes, also observed by Xiao et al. (2005), in a 718 alloy after room temperature fatigue deformation.

After solution annealing at $1150 \text{ }^\circ\text{C}$ during one hour, the specimen become free of Cr_{23}C_6 carbides and the average grain size is about $90 \text{ }\mu\text{m}$. Many annealing twins appear during solid solution treatment as can be seen in Fig. 1. Annealing twins, are easily formed during grain growth when FCC metals have a low stacking fault energy as mentioned by Park et al. (2007). After the three SS heat treatments, the grain size ranges from 75 to $150 \text{ }\mu\text{m}$ (Table 4).

After annealing at $900 \text{ }^\circ\text{C}$ during 17 min, a change in the morphology of the precipitates is observed, with the presence of a continuous layer of M_{23}C_6 at grain boundaries, instead of coarse individual precipitates (Fig. 2). After precipitation treatment, the average grain size slightly increases from 90 to $105 \text{ }\mu\text{m}$.

The influence of Cr_{23}C_6 carbides on the mechanical behavior will be quantified in Section 3.2 by comparing the specimens referred as SS-90 μm and FP. The grain size effects on the yield stress and strain hardening will be also quantified for three grain size levels corresponding to the specimens SS-75 μm , SS-90 μm and SS-150 μm .

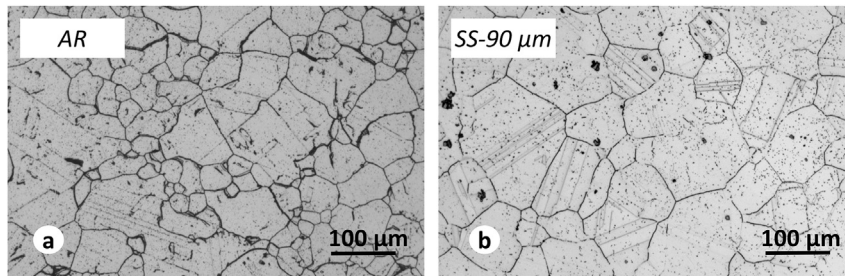


Fig. 1. microstructures of alloy NY690 after electro-etching for as-received (a) and solution-annealed (b) specimens.

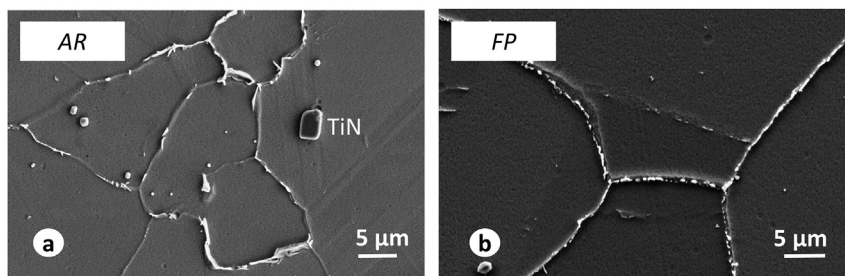


Fig. 2. SEM micrographs of precipitates for as-received (a) and fully precipitated (b) specimen.

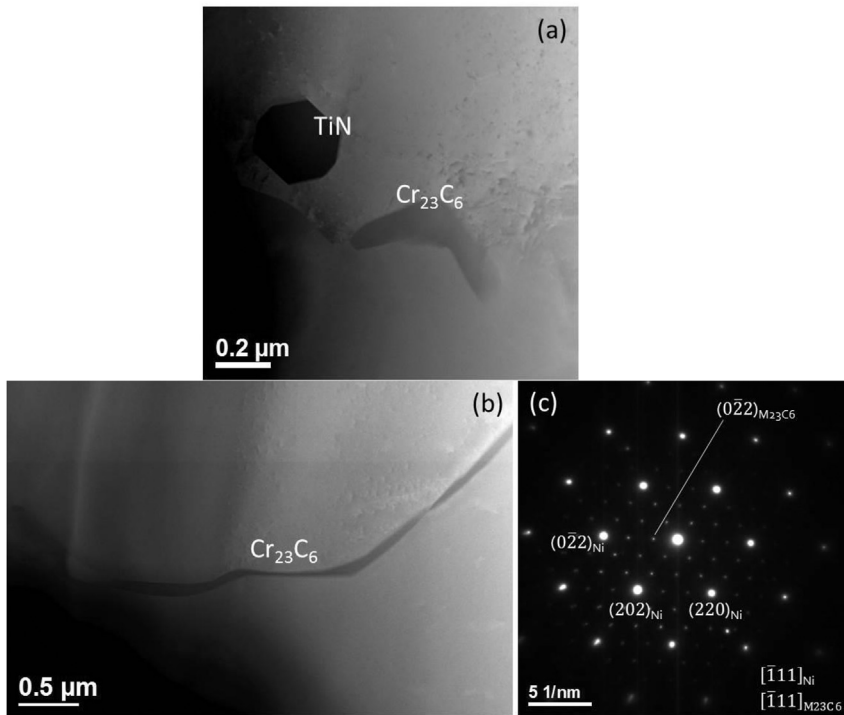


Fig. 3. (a) TEM HAADF micrographs of as-received specimen, with the presence of $M_{23}C_6$ and TiN precipitates, located at grain boundaries, (b) for some boundaries a continuous $M_{23}C_6$ film is observed. (c) Selected Area Diffraction pattern of a coherent $M_{23}C_6$ precipitate, the matrix is oriented $[-111]$.

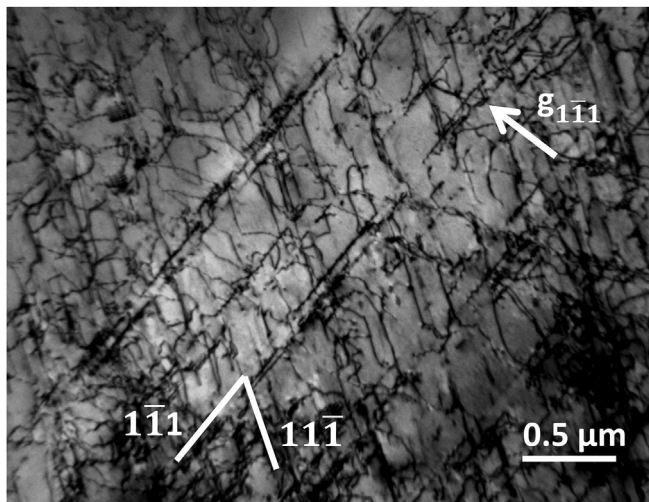


Fig. 4. Dislocation structure in the as-received sample. Dislocations lines are observed on $\{111\}$ planes.

Table 4
Average grain size of AR, solution annealed and fully precipitated specimens.

Microstructural state	Heat treatment	Average grain size (μm)
As-received (AR)		50
Solution annealed (SS-75 μm)	AR + 15 min at 1150 °C	75
Solution annealed (SS-90 μm)	AR + 60 min at 1150 °C	90
Solution annealed (SS-150 μm)	AR + 90 min at 1200 °C	150
Fully precipitated (FP)	AR + 60 min at 1150 °C + 17 min at 900 °C	105

3.2. Uniaxial loading

3.2.1. Effects of the microstructure on the tensile behavior

The effects of grain size and carbides on the tensile flow behavior have been studied at 25 °C (Fig. 5) and at 750 °C (Fig. 6). The influence of the grain size on the yield stress (at a plastic strain of 0.2%) has been investigated for three average grain sizes respectively 75, 90 and 150 μm at 25 °C and at a strain rate of $5 \times 10^{-4} \text{ s}^{-1}$ (Table 5). It can be concluded that the effect of the grain size is here relatively low, which can be explained by the large size of the grains. Note also that there is no effect of chromium carbides on the yield stress since precipitation occurs at the grain boundaries (Table 5). At room temperature, see Fig. 5, the strain hardening is almost linear particularly after solution annealing treatment. As shown in Fig. 5a the strain hardening rate decreases slightly when the grain size increases, whereas no effect of the presence of chromium carbides at the grain boundaries can be observed in Fig. 5b.

At 750 °C for a strain rate of $5 \times 10^{-4} \text{ s}^{-1}$, grain size and chromium carbides have also little effect on the yield stress (Table 6). The hardening behavior is mainly modified after the solution annealing treatment which decreases the dislocation density. A lower dislocation density can promote the dynamic strain aging as shown in Fig. 6. When dynamic strain aging occurs, the strain hardening rate is almost constant up to a true strain of 0.10 at 750 °C to reach the steady-state regime. The steady-state stress increases slightly when grain size increases, from 300 MPa for a grain size of 75 μm –320 MPa for a grain size of 150 μm .

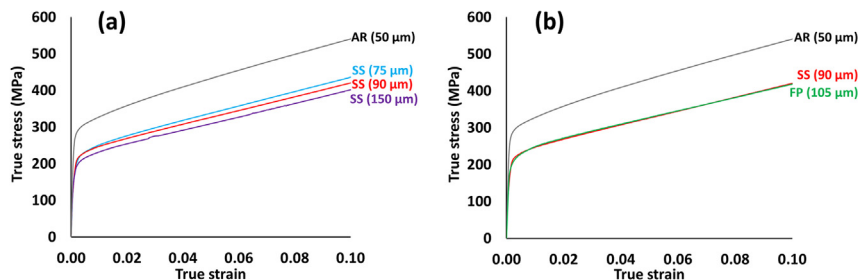


Fig. 5. Influence of average grain size (a) and chromium carbides (b) on the tensile behavior at 25 °C and at a strain rate of $5 \times 10^{-4} \text{ s}^{-1}$.

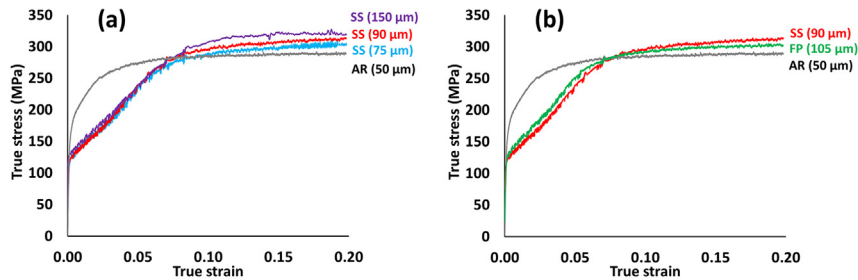


Fig. 6. Influence of average grain size (a) and chromium carbides (b) on the tensile behavior at 750 °C and a strain rate of $5 \times 10^{-4} \text{ s}^{-1}$.

Table 5

Influence of average grain size and chromium carbides at a strain rate of $5 \times 10^{-4} \text{ s}^{-1}$ on the yield stress and on the strain hardening rate at 25 °C.

Microstructural state	Average grain size (μm)	Yield stress 0.2% (MPa)	Strain hardening rate (MPa)
As-received (AR)	50	305 ± 10	2065 ± 25
Solution annealed (SS-75 μm)	75	225 ± 10	1970 ± 25
Solution annealed (SS-90 μm)	90	220 ± 15	1885 ± 30
Solution annealed (SS-150 μm)	150	205 ± 10	1900 ± 30
Fully precipitated (FP)	105	225 ± 15	1850 ± 15

Table 6

Effects of average grain size and chromium carbides on the yield stress and on the steady-state stress at 750 °C and at a strain rate of $5 \times 10^{-4} \text{ s}^{-1}$.

Microstructural state	Average grain size (μm)	Yield stress 0.2% (MPa)	Steady-state stress (MPa)
As-received (AR)	50	150 ± 10	280 ± 5
Solution annealed (SS-75 μm)	75	124 ± 2	298 ± 2
Solution annealed (SS-90 μm)	90	126 ± 3	306 ± 2
Solution annealed (SS-150 μm)	150	134 ± 2	322 ± 2
Fully precipitated (FP)	105	129 ± 1	299 ± 2

3.2.2. Effects of temperature

True stress vs. true strain curves are plotted between 25 and 1000 °C at a strain rate of 10^{-4} s^{-1} in Fig. 7. Between 25 and 600 °C, two stages of strain hardening occur as shown in Fig. 8. The first stage, namely stage I, is characterized by a high hardening rate that decreases abruptly up to 2000 MPa. The work hardening is almost constant for strain larger than 0.02 in the second stage (stage II). Above 600 °C, a third stage (stage III) appears in Fig. 8 in which the hardening rate decreases linearly when the stress increases and can be due to the beginning of dynamic recovery.

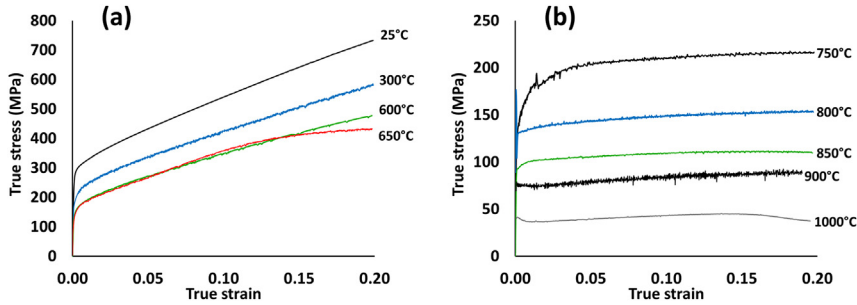


Fig. 7. Tensile true stress – true strain curves for as-received specimen deformed at a strain rate of 10^{-4} s^{-1} between 25 and 650 °C (a) and between 750 and 1000 °C (b).

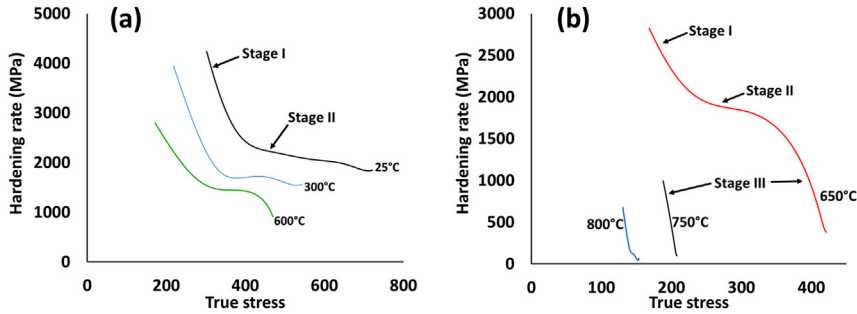


Fig. 8. Strain hardening rate Θ versus true stress between 25 and 600 °C (a) and between 650 and 800 °C (b) at a strain rate of 10^{-4} s^{-1} .

3.2.3. Effects of strain-rate

The compressive flow stress-strain response is plotted as a function of the strain rate between 10^{-3} and 10^{-1} s^{-1} in Fig. 9a. The strain rate sensitivity is quite small at room temperature in quasi-static regime. The strain rate sensitivity is defined as:

$$\lambda = \left. \frac{\partial(\ln \sigma)}{\partial(\ln \dot{\epsilon}_p)} \right|_{\epsilon, T} \tag{1}$$

As it can be seen in Table 7, the strain rate sensitivity decreases when the plastic strain increases. In strain-rate jump tensile experiments (Fig. 9b), the stress increase is about 10 MPa during each strain-rate jump.

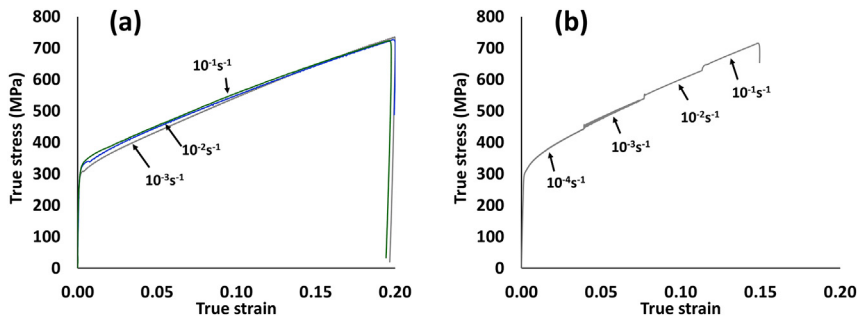


Fig. 9. True stress–strain curves of as-received NY690 at different strain rates in compression (a) and strain-rate jump tensile curves (b) at 25 °C.

Table 7
Strain rate sensitivity at different plastic strain levels and at room temperature.

Plastic strain λ	0.03	0.05	0.10	0.15
	0.010	0.011	0.005	0.001

At 750 °C, whereas the strain rate has little influence on the yield stress, it has a significant influence on the work hardening and the steady-state stress (Fig. 10). Indeed, the value of the latter is 205 MPa at a strain rate of 10^{-4} s^{-1} and 435 MPa at a strain rate of $5 \times 10^{-3} \text{ s}^{-1}$. Whereas stage III appears only for a strain rate of 10^{-4} s^{-1} , stage I and II are also present at a strain rate of 10^{-3} and $5 \times 10^{-3} \text{ s}^{-1}$.

The strain hardening is relatively low at 900 °C and the stress is mainly a function of the strain rate. An abnormal variation occurs on the strain-stress curve at the beginning of the plastic deformation particularly at a strain rate of $5 \times 10^{-3} \text{ s}^{-1}$ (Fig. 11a). These variations are clearly caused by uncontrolled strain rate at the beginning of the tensile test (Fig. 11b). To calculate the strain rate, the strain-times curves are fitted by a polynomial function by least-squares method in order to minimize noise. At a strain rate of $8 \times 10^{-3} \text{ s}^{-1}$, the stress increase is also caused by the strain rate increase. Hardening seems to be significant only at a strain rate of $4 \times 10^{-2} \text{ s}^{-1}$.

In this section, the effects of plastic strain rate, temperature and of the microstructure on mechanical behavior have been detailed. At 25 °C and 750 °C, the yield stress and the strain hardening are not affected by the grain size and the presence of chromium carbides. As a consequence, the yield stress is assumed to be a function of the initial dislocation density and the main mechanism for the strain hardening is supposed to be the interaction between dislocations.

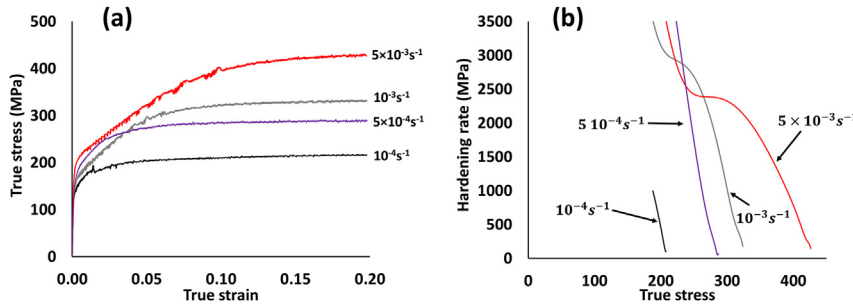


Fig. 10. Tensile stress–strain curves of as-received NY690 (a) and hardening rates (b) at different strain rate and at 750 °C.

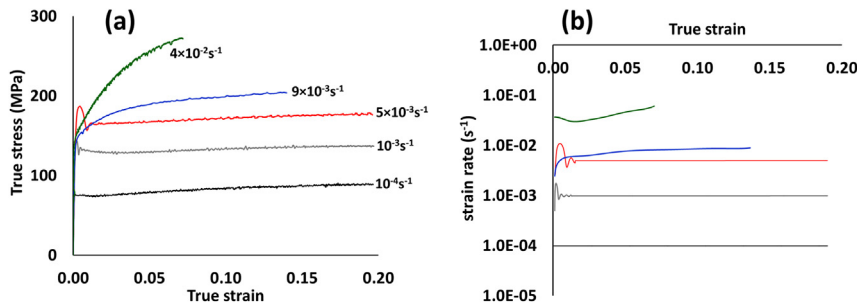


Fig. 11. Tensile stress–strain curves of as-received NY690 (a) and calculated strain rates (b) at 900 °C.

4. Modeling and discussion

4.1. Modeling

The total strain rate tensor $\dot{\epsilon}_{ij}$ is given by the sum of the elastic strain rate $\dot{\epsilon}_{ij}^e$ and the plastic strain rate $\dot{\epsilon}_{ij}^p$. The cumulated plastic strain rate $\dot{\epsilon}_p$ is given by the following equation in the general case (multi-axial loading):

$$\dot{\epsilon}_p = \sqrt{\frac{2}{3} \dot{\epsilon}_{ij}^p \dot{\epsilon}_{ij}^p} \tag{2}$$

The von Mises equivalent stress σ is related to the deviatoric stress tensor S_{ij} :

$$\sigma = \sqrt{\frac{3}{2} S_{ij} S_{ij}} \tag{3}$$

Mecking and Kocks (1981), Estrin and Mecking (1984), Estrin (1998), Kocks and Mecking (2003) and Estrin (2007) proposed a phenomenological treatment of the plastic deformation by using only one parameter ρ representing the dislocation density. The dependence of the equivalent flow stress σ on the plastic strain rate $\dot{\epsilon}_p$ and on the temperature T , for a given microstructure, is given by the following equation:

$$\sigma = \sigma(\rho, \dot{\epsilon}_p, T) = \hat{\sigma}(\rho) \left(\frac{\dot{\epsilon}_p}{\dot{\epsilon}_0^G(T)} \right)^{\frac{1}{m}} \tag{4}$$

where $\hat{\sigma}(\rho)$ is the stress required for a dislocation to glide, m is an exponent and $\dot{\epsilon}_0^G(T)$ is a reference shear strain characteristic of the gliding mechanism. This can be represented by the Arrhenius equation for which $\dot{\epsilon}_{00}^G$ is a constant and Q_G is the activation energy for the gliding mechanism:

$$\dot{\epsilon}_0^G = \dot{\epsilon}_{00}^G \exp\left(-\frac{Q_G}{R_g T}\right) \tag{5}$$

According to the KME (Kocks–Mecking–Estrin) model, the dislocation density ρ evolves with the plastic strain as:

$$\frac{d\rho}{d\epsilon_p} = h\sqrt{\rho} - r\rho \tag{6}$$

where h is a storage rate term and r is the dynamic recovery term, which can be expressed as:

$$r = r_0 \left(\frac{\dot{\epsilon}_p}{\dot{\epsilon}_0^C} \right)^{-\frac{1}{n}} \tag{7}$$

where n is an exponent, r_0 a constant and $\dot{\epsilon}_0^C$ is a reference shear strain characteristic of the climbing mechanism that can be represented again by an Arrhenius equation for which $\dot{\epsilon}_{00}^C$ is a constant and Q_C is an activation energy for the climbing mechanism:

$$\dot{\epsilon}_0^C = \dot{\epsilon}_{00}^C \exp\left(-\frac{Q_C}{R_g T}\right) \tag{8}$$

The dynamic recovery coefficient r is finally expressed as follows:

$$r = K_r (\dot{\epsilon}_p)^{-1/n} \times \exp\left(-\frac{Q_C}{nR T}\right) \tag{9}$$

with

$$K_r = r_0 (\dot{\epsilon}_{00}^C)^{+1/n} \tag{10}$$

The average dislocation density ρ is used as a governing parameter by considering a plastically isotropic polycrystalline material and isotropic hardening only is considered. Assuming a periodic dislocation network, a similar equation than in Taylor (1934) is used to link the flow stress and the dislocation density:

$$\hat{\sigma} = \hat{\sigma}_y^d + \hat{R} \tag{11}$$

where $\hat{\sigma}_y^d$ is the contribution of the dislocation network to the yield stress. It is a function of the initial dislocation density ρ_0 for which M is the Taylor factor, μ is the shear modulus and b is the amplitude of the Burgers vector:

$$\hat{\sigma}_y^d = M\alpha\mu b\sqrt{\rho_0} \tag{12}$$

leaving for the strain hardening \widehat{R} :

$$\widehat{R} = M\alpha\mu b(\sqrt{\rho} - \sqrt{\rho_0}) \quad (13)$$

The initial dislocation density ρ_0 is $3 \times 10^{13} \text{ m}^{-2}$, this value has been measured by TEM (cf. Section 3.1). For the solution annealed and fully precipitated specimens, the initial dislocation density is estimated to $1.5 \times 10^{13} \text{ m}^{-2}$ at 25 °C using Eq. (12). The constant related to the forest hardening α is chosen equal to 0.5 (Madec et al., 2002).

For the case of a constant plastic strain rate, by combining Eqs. (6), (12) and (13), the well-known Voce equation (1948) can be obtained in stage III:

$$R = (\sigma_{SS} - \sigma_y) \times \left(1 - \exp\left(-\frac{\varepsilon_p}{\varepsilon_{tr}}\right)\right) \quad (14)$$

The transient strain ε_{tr} determine the rate at which the steady-state stress σ_{SS} is reached:

$$\varepsilon_{tr} = \frac{\sigma_{SS}}{\Theta_{II}} = \frac{2}{r} \quad (15)$$

The steady-state stress can be written as follows:

$$\sigma_{SS} = K(\dot{\varepsilon}_p)^{\lambda_{SS}} \exp\left(\frac{Q}{RT}\right) \quad (16)$$

where

$$K = M\alpha\mu b \frac{h}{r_0} (\varepsilon_{00}^G)^{-1/m} (\varepsilon_{00}^C)^{-1/n} \quad (17)$$

$$\lambda_{SS} = \frac{1}{n} + \frac{1}{m} \quad (18)$$

and

$$Q = \frac{Q_c}{n} + \frac{Q_G}{m} \quad (19)$$

The activation energies Q and Q_c/n have been fitted respectively to 68 kJ/mol and 108 kJ/mol (Fig. 12).

The strain-rate sensitivity of σ_{SS} increases from 0 at 600 °C to 0.21 at 750 °C (Table 8). To account for this drastic increase of λ_{SS} as a function of the temperature, a Gaussian error function is used in Eq. (20).

$$\lambda_{SS} = \frac{\lambda_{SS0}}{2} [1 + \text{erf}(A \times T + B)] \quad (20)$$

By combing Eqs. (4), (5) and (12), the yield stress can be obtained:

$$\sigma_{y/\mu} = M\alpha b \sqrt{\rho_0} \left(\frac{\dot{\varepsilon}_p}{\dot{\varepsilon}_{00}^G}\right)^{\frac{1}{m}} \exp\left(+\frac{Q_G}{mR_gT}\right) \quad (21)$$

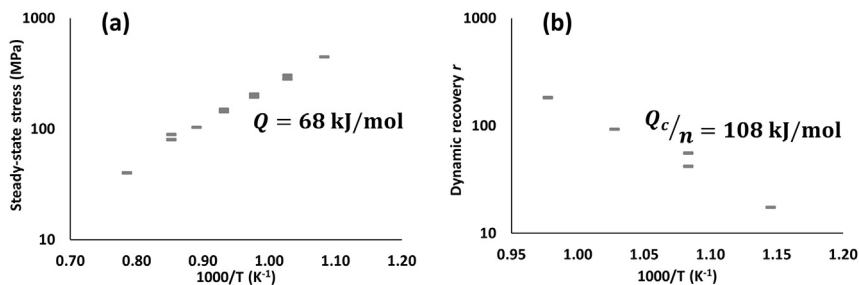


Fig. 12. Effects of temperature at a strain rate of 10^{-4} s^{-1} on steady-state stress (a) and dynamic recovery parameter (b).

Table 8
Strain-rate sensitivity at steady-state as function of temperature.

Temperature	600	650	700	750	900
λ_{ss}	0	0.10	0.18	0.21	0.20

Below 800 °C, the yield stress can be simplified as follows with a smaller activation energy Q_Y :

$$\sigma_y/\mu = M\alpha b\sqrt{\rho_0}\exp\left(+\frac{Q_Y}{R_gT}\right) \tag{22}$$

The stage II hardening rate is given by:

$$\Theta_{II} = \frac{1}{2}\alpha\mu bMh\left(\frac{\dot{\epsilon}_p}{\dot{\epsilon}_{G00}}\right)^{\frac{1}{m}}\exp\left(\frac{Q_G}{mRT}\right) \tag{23}$$

Below 650 °C, the stage II hardening rate is mainly a function of the shear modulus and the ratio Θ/μ is about $(2.4\pm 0.1)10^{-2}$. As a consequence, Eq. (23) can be simplified as follows:

$$\Theta_{II} = \frac{1}{2}\alpha\mu bMh_0 \tag{24}$$

The strain hardening relationship is as follows in stage II:

$$R = \sigma - \sigma_y = \left(\frac{1}{2}\alpha\mu bMh_0\right)\epsilon_p \tag{25}$$

Two cases have been analyzed to simulate the mechanical behavior: i) forest hardening regime ii) competition between forest hardening and dynamic recovery. The forest hardening regime occurs mainly below 650 °C (stage II) whereas the competition between the forest hardening and the dynamic recovery happens between 650 °C and 900 °C (stage III). The transition between stage II and stage III happens at a threshold temperature *i.e.* 650 °C for which the strain rate sensitivity and the dynamic recovery parameters drastically increase.

The final set of equations of the model is recalled in Table 9, and the dependence of parameters as a function of the temperature and the strain rate in Table 10. The values of physical properties and adjustable parameters are given in Table 11.

Table 9
Constitutive equations of the model.

T (°C)	Yield stress	Hardening
25–650	$\sigma_y = M\alpha\mu b\sqrt{\rho_0}\exp\left(+\frac{Q_Y}{R_gT}\right)$	$R = \frac{M\alpha\mu b h_0}{2}\epsilon_p$
650–800	$\sigma_y = M\alpha\mu b\sqrt{\rho_0}\exp\left(+\frac{Q_Y}{R_gT}\right)$	$R = (\sigma_{ss} - \sigma_y) \times \left(1 - \exp\left(-\frac{r}{2}\epsilon_p\right)\right)$
800–1000	$\sigma_y = M\alpha\mu b\sqrt{\rho_0}\left(\frac{\dot{\epsilon}_p}{\dot{\epsilon}_{G00}}\right)^{\frac{1}{m}}\exp\left(+\frac{Q_G}{mR_gT}\right)$	$R = (\sigma_{ss} - \sigma_y) \times \left(1 - \exp\left(-\frac{r}{2}\epsilon_p\right)\right)$

Table 10
Expression for the model parameters as a function of the temperature and the strain rate.

Parameter	Equation
Forest hardening coefficient	$h_0 = 130 \times 10^6 \text{ m}^{-1}$
Dynamic recovery coefficient	$r = K_r(\dot{\epsilon}_p)^{-\frac{1}{n}} \times \exp\left(-\frac{Q_r}{nR_gT}\right)$
Strain-rate sensitivity	$\lambda_{ss} = \frac{\lambda_{ss0}}{2} [1 + \text{erf}(A \times T + B)]$
Steady-state stress	$\sigma_{ss} = K(\dot{\epsilon}_p)^{\lambda_{ss}} \exp\left(\frac{Q}{RT}\right)$

Table 11

Values of physical properties and adjustable parameters used to compare with experimental data for alloy NY690.

Parameter	Value
<i>Physical properties</i>	
M	3 (Sinclair et al., 2006)
α	0.5 (Madec et al., 2002)
E	$210 - 0.017 \times T - 7.9 \times 10^{-5} \times T^2$ (GPa) ^a
μ	$80.7 - 0.0266 \times T$ (GPa) ^b
b	0.252 nm^c
<i>Adjustable parameters (fitted to experimental data)</i>	
h_0	$130 \times 10^6 \text{ m}^{-1}$
K	0.52 MPa
Q	68 kJ/mol
Q_C	330 kJ/mol
Q_G	395 kJ/mol
Q_Y	1.6 kJ/mol
m	7.0
n	3.05
$\dot{\epsilon}_{00}^G$	$6.1 \times 10^{14} \text{ s}^{-1}$
λ_{SS0}	0.21
K_r	2.7×10^6
A	0.016 K^{-1}
B	-15.2

^a Temperature in °C, values measured in this study.

^b Temperature in °C, <http://www.specialmetals.com/documents/Inconel%20alloy%20690.pdf>.

^c Value measured by TEM.

4.2. Modeling results

The yield stress can be predicted at 25 °C and at 750 °C by considering only the initial dislocation density for solution-annealed specimens (Fig. 13). At 25 °C, the simulated curve of SS-90 μm specimen is very close to the experimental result. Indeed, the hardening rate is hardly dependent of the grain size. For large grain sizes (more than 50 μm), the effect of them on strain hardening is clearly negligible as mentioned by Sinclair et al. (2006).

At 750 °C, the lower initial density dislocation ($1.5 \times 10^{13} \text{ m}^{-2}$) of SS specimen promotes the dynamic strain aging (DSA) which leads to a constant hardening rate of about 2300 MPa. This hardening rate is significantly higher than the stage II hardening rate which is about 1500 MPa at 750 °C. DSA occurs mainly between 300 °C and 750 °C and the major serrations are produced between 500 °C and 750 °C. The dynamic strain aging has been also observed between 300 °C and 800 °C in other superalloys by Chaboche et al. (2013). DSA occurs in a material-specific range of loading rate and temperature associated with “repeated” interaction between (mobile) dislocations and solute atoms as mentioned by Klusemann et al. (2015). In the case of complex multi-axial loadings involved during multi-pass welding, the occurrence of DSA is hardly probable so the interactions between dislocations and solute atoms have been neglected. The simulated steady-stress is also slightly lower than the experimental steady-stress since grain size slightly increases the steady-stress (Figs. 6 and 13) due to the grain-boundary sliding.

The simulated yield stress is very close to the experimental results between 25 °C and 1000 °C at a strain rate of 10^{-4} s^{-1} for AR specimens. Stage II hardening is only a function of the forest hardening coefficient and the shear modulus. Slight deviations between simulated stress in stage II and experimental stress arises from the elastic–plastic transition (Fig. 14a). Transition between stage II and stage III occurs at about 650 °C due to the activation of the gliding and the climbing of dislocations as mentioned by Frost and Ashby (1982) and Estrin (2007).

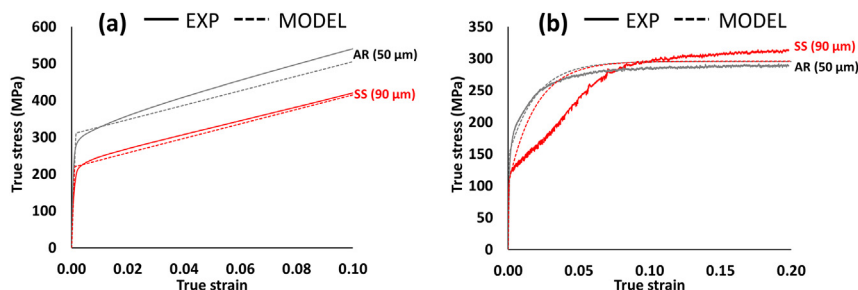


Fig. 13. Experimental and simulated strain curves at 25 °C (a) and at 750 °C (b) and at a strain rate of $5 \times 10^{-4} \text{ s}^{-1}$ for AR ($\rho_0 = 3.0 \times 10^{13} \text{ m}^{-2}$) and SS-90 μm ($\rho_0 = 1.5 \times 10^{13} \text{ m}^{-2}$).

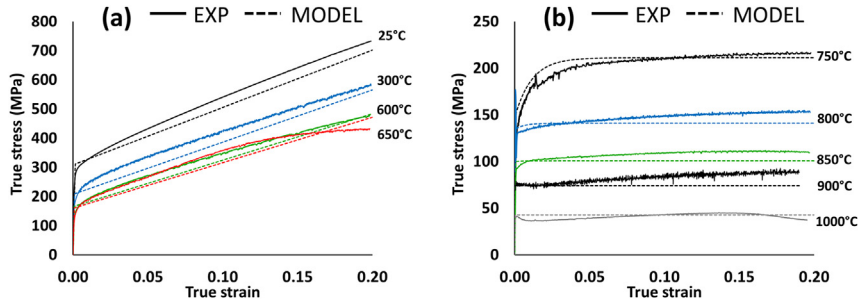


Fig. 14. Experimental and simulated strain curves between 25 °C and 650 °C (a) and between 750 °C and 1000 °C (b) at a strain rate of 10^{-4} s^{-1} for AR specimens.

True stress is correctly predicted for AR specimens between 750 °C and 1000 °C using Voce's equation (Eq. (14)). The transient strain $2/r$ characterizes the rate at which the steady-state stress σ_{SS} is reached in stage III (Eq. (9)). Indeed, dynamic recovery is thermally activated with an energy activation Q_C/n of 108 kJ/mol. This activation energy is very close to the activation energy of vacancy migration (106 kJ/mol), determined by Chambon and Caplain (1974) for Ni30Fe alloy, which is involved in the dislocation climbing. The dislocation climbing promotes the annihilation of dislocations as mentioned by Frost and Ashby (1982), Estrin (2007) and recently by Galindo-Nava and Rivera-Díaz-del-Castillo (2013). The activation energy of the steady-stress reported by Bi et al. (2010) for alloy NY690 is 357 kJ/mol which is the average value of Q_C and Q_G in this work.

The strain-rate plays also a major role on the strain hardening which is illustrated in Fig. 15. Higher strain rate delays the stage III and the steady-state regime by decreasing the dynamic recovery parameter and increasing the steady-state stress. The dislocation annihilation is easier at lower strain rates due to the diffusion of vacancies. As mentioned by Khan and Liu (2012) for another FCC alloy (Al 2024-T351), the strain rate sensitivity increases as a function of temperature above a threshold temperature which is 650 °C. A peak flow stress is seen in Figs. 11 and 15 at 900 °C for a strain rate of 10^{-3} s^{-1} and $5 \times 10^{-3} \text{ s}^{-1}$, respectively, which is clearly due to a higher strain rate at the beginning of plastic deformation. At 900 °C, the transition between stage III and the pure recovery regime as a function of strain rate is correctly predicted and the main deviation is due to strain rate variations.

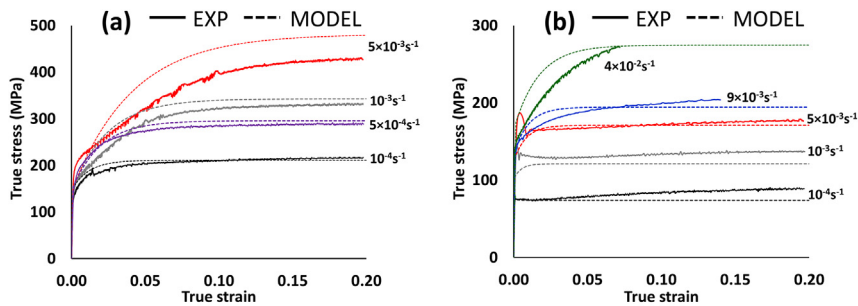


Fig. 15. Experimental and simulated strain curves at 750 °C (a) and at 900 °C (b) at different strain rates for AR specimens.

5. Conclusions

NY690 samples were subjected to a wide range of isothermal heat treatments leading to various microstructural states and grain sizes. At 25 °C and at 750 °C, the grain size and chromium carbides have little influence on the yield stress and the strain hardening. Indeed, the yield stress is mainly a function of dislocation density and the main mechanism for the strain hardening is the interaction between dislocations. DSA occurs mainly between 500 and 700 °C in tensile loading and hardly occurs in complex multi-axial loading happening during the multi-pass welding. For the studied range of temperature (25–1100 °C) and strain rate (10^{-4} to $5 \times 10^{-3} \text{ s}^{-1}$) the mechanical behavior can thus be divided in three regimes: i) between 25 °C and 600 °C: strain hardening predominant and almost linear with negligible strain rate effect, ii) between 600 and 800 °C: transition of mechanical behavior with thermal activation of dynamic recovery and strain rate sensitivity, iii) above 800 °C: viscoplastic behavior and constant strain rate sensitivity with negligible strain hardening.

The KME formalism is thus adapted for the wide range of temperature and strain rate to predict the mechanical behavior and residual stresses of the alloy during and after welding. Furthermore, the simplicity of the proposed model allows for an easy implementation in Finite Element codes.

Acknowledgements

The authors want to acknowledge Florian Mercier and Thierry Douillard for technical support. Thanks are due to the CLYM (Centre Lyonnais de Microscopie) in Lyon for access to the microscope.

Nomenclature

σ	von Mises equivalent stress
S_{ij}	deviatoric stress tensor
$\bar{\sigma}$	stress required for a dislocation to glide
σ_y	yield stress
$\bar{\sigma}_y^d$	contribution of the dislocation network of the yield stress
σ_{ss}	steady-state stress
\bar{R}	strain hardening as a function of dislocation density
R	strain hardening as a function of plastic strain
Θ	strain hardening rate
Θ_{II}	stage II strain hardening rate
ε	true strain
ε_p	true plastic strain
ε_{tr}	transient strain
$\dot{\varepsilon}_{ij}$	total strain rate tensor
$\dot{\varepsilon}_{ij}^e$	elastic strain rate tensor
$\dot{\varepsilon}_{ij}^p$	plastic strain rate tensor
$\dot{\varepsilon}_p$	plastic strain rate
$\dot{\varepsilon}_0^G$	reference shear strain characteristic of gliding mechanism
$\dot{\varepsilon}_{00}^G$	pre-exponential factor for the reference shear strain of gliding mechanism
$\dot{\varepsilon}_0^C$	reference shear strain characteristic of climbing mechanism
$\dot{\varepsilon}_{00}^C$	pre-exponential factor for the reference shear strain of climbing mechanism
T	absolute temperature (K)
R_g	ideal gas constant
Q	activation energy of steady-state stress
Q_c	activation energy for climbing mechanism
Q_G	activation energy for gliding mechanism
Q_y	activation energy of yield stress
ρ	average dislocation density
ρ_0	initial average dislocation density
r_0	constant for the expression of dynamic recovery coefficient
M	Taylor factor
α	constant related to the forest hardening
μ	shear modulus
b	amplitude of the Burgers vector
k_g	Hall-Petch constant
d	average grain size
h	strain hardening coefficient
h_0	constant for the expression of strain hardening coefficient
r	dynamic recovery coefficient
r_0	constant for the expression of dynamic recovery coefficient
K_r	pre-exponential factor for the expression of dynamic recovery coefficient
λ	strain rate sensitivity
λ_{ss}	strain rate sensitivity of steady-state stress
λ_{ss0}	asymptotic value of λ_{ss}
A	constant for the determination of λ_{ss}
B	constant for the determination of λ_{ss}
m	exponent for the expression of flow stress
n	exponent for the expression of dynamic recovery
K	constant for the calculation of steady-state stress

References

- Bardel, D., Perez, M., Nelias, D., Dancette, S., Chaudet, P., Massardier, V., 2015. Cyclic behavior of a 6061 aluminium alloy: coupling precipitation and elastoplastic modeling. *Acta Mater.* 83, 256–268.
- Bergström, Y., 1970. A dislocation model for the stress-strain behaviour of polycrystalline α -Fe with special emphasis on the variation of the densities of mobile and immobile dislocations. *Mater. Sci. Eng.* 5, 193–200.
- Bi, Z., Zhang, M., Dong, J., Luo, K., Wang, J., 2010. A new prediction model of steady state stress based on the influence of the chemical composition for nickel-base superalloys. *Mater. Sci. Eng. A* 527, 4373–4382.
- Chaboche, J.L., 2008. A review of some plasticity and viscoplasticity constitutive theories. *Int. J. Plast.* 24, 1642–1693.
- Chaboche, J.-L., Gaubert, A., Kanouté, P., Longuet, A., Azzouz, F., Mazière, M., 2013. *Int. J. Plast.* 46, 1–22.
- Chambon, W., Caplain, A., 1974. Study of vacancies in very low concentration in an iron 70 at. % nickel alloy by the magnetic anisotropy method. *Acta Metall.* 22, 357–366.
- Choi, S.H., Kim, E.-Y., Woo, W., Han, S.H., Kwak, J.H., 2013. The effect of crystallographic orientation on the micromechanical deformation and failure behaviors of DP980 steel during uniaxial tension. *Int. J. Plast.* 45, 85–102.
- Csanádi, T., Chinh, N.Q., Gubicza, J., Vörös, G., Langdon, T.G., 2014. Characterization of stress–strain relationships in Al over a wide range of testing temperatures. *Int. J. Plast.* 54, 178–192.
- Diano, P., Muggeo, A., Van Duysen, J.C., Guttman, M., 1989. Relationship between microstructure and mechanical properties of alloy 690 tubes for steam generators. *J. Nucl. Mater.* 168, 290–294.
- DuPont, J.N., Lippold, J.C., Kiser, S.D., 2009. *Welding Metallurgy and Weldability of Ni-base Alloys*. Wiley & Sons, Hoboken.
- Estrin, Y., 1998. Dislocation theory based constitutive modeling: foundations and applications. *J. Mater. Process. Technol.* 80–81, 33–39.
- Estrin, Y., 2007. Constitutive modelling of creep of metallic materials: some simple recipes. *Mater. Sci. Eng. A* 463, 171–176.
- Estrin, Y., Mecking, H., 1984. A unified phenomenological description of work hardening and creep based on one-parameter models. *Acta Metall.* 32, 57–70.
- Frost, H.J., Ashby, M.F., 1982. *Deformation-mechanism Maps: the Plasticity and Creep of Metals and Ceramics*. Pergamon Press, Oxford, p. 166.
- Galindo-Nava, E.L., Rivera-Díaz-del-Castillo, P.E.J., 2013. Thermostatistical modeling of hot deformation in FCC metals. *Int. J. Plast.* 47, 202–221.
- Guo, S., Li, D., Pen, H., Guo, Q., Hu, J., 2011. Hot deformation and processing maps of Inconel 690 superalloy. *J. Nucl. Mater.* 410, 52–58.
- Harrod, D.L., Gold, R.E., Jacko, R.J., 2001 July. Alloy optimization for PWR steam generator heat-transfer tubing. *JOM* 14–17.
- Jung, K.-H., Kim, D.-K., Im, Y.-T., Lee, Y.S., 2013. Prediction of the effects of hardening and texture heterogeneities by finite element analysis based on the Taylor model. *Int. J. Plast.* 42, 120–140.
- Kai, J.J., Yu, G.P., Tsai, C.H., Liu, M.N., Yao, S.C., 1989. The effects of heat treatment on the chromium depletion, precipitate evolution, and corrosion resistance of INCONEL alloy 690. *Metall. Trans.* 20A, 2057–2067.
- Khan, A.S., Liu, H., 2012. Variable strain rate sensitivity in an aluminum alloy: response and constitutive modelling. *Int. J. Plast.* 36, 1–14.
- Klusemann, B., Fischer, G., Böhlke, T., Svendsen, B., 2015. Thermomechanical characterization of Portevin–Le Châtelier bands in AlMg3 (AA5754) and modeling based on a modified Estrin–McCormick approach. *Int. J. Plast.* 67, 192–216.
- Kocks, U.F., Mecking, H., 2003. Physics and phenomenology of strain hardening: the FCC case. *Prog. Mater. Sci.* 48, 171–273.
- Li, H., Xia, S., Zhou, B., Peng, J., 2013. The growth mechanism of grain boundary carbide in alloy 690. *Mater. Charact.* 81, 1–6.
- Mader, R., Devindre, B., Kubin, L.P., 2002. From dislocation junctions to forest hardening. *Phys. Rev. Lett.* 89, 255508.
- Mecking, H., Kocks, U.F., 1981. Kinetics of flow and strain-hardening. *Acta Metall.* 29, 1865–1875.
- Park, N.K., Kim, J.J., Chai, Y.S., Lee, H.S., 2007. Microstructural evolution of Inconel 690 alloy for steam generator tubes. *Key Eng. Mater.* 353–358, 1609–1613.
- Puchi-Cabrera, E.S., Staia, M.H., Guérin, J.D., Lesage, J., Dubar, M., Chicot, D., 2013. Analysis of the work-hardening behavior of C-Mn steels deformed under hot-working conditions. *Int. J. Plast.* 51, 145–160.
- Reed, R.C., 2006. *The Superalloys: Fundamentals and Applications*. Cambridge University Press, Cambridge.
- Sabol, G.P., Stickler, R., 1969. Microstructure of nickel-based superalloys. *Phys. Stat. Sol.* 35, 11.
- Sellars, C.M., McTegart, W.J., 1966. On the mechanism of hot deformation. *Acta Metall.* 14, 1136–1138.
- Sinclair, C.W., Poole, W.J., Bréchet, Y., 2006. A model for the grain size dependent work hardening of copper. *Scr. Mater.* 55, 739–742.
- Taylor, G.I., 1934. The mechanism of plastic deformation of crystals. Part I. Theoretical. *Proc. R. Soc. Lond. A* 45, 362–387.
- Venkatesh, V., Rack, H.J., 1998. Elevated temperature hardening of INCONEL 690. *Mech. Mater.* 30, 69–81.
- Voce, E.J., 1948. The relationship between stress and strain for homogeneous deformations. *Inst. Met.* 74, 537.
- Wang, J.D., Gan, D., 2001. Effects of grain boundary carbides on the mechanical properties of Inconel 600. *Mater. Chem. Phys.* 70, 124–128.
- Wu, H.Y., Sun, P.-H., Zhu, F.J., Wang, S.C., Wang, W.R., Wang, C.C., Chiu, C.H., 2012. Tensile flow behavior in Inconel 600 alloy sheet at elevated temperatures. *Procedia Eng.* 36, 114–120.
- Xiao, L., Chen, D.L., Chaturvedi, M.C., 2005. Shearing of γ ' precipitates and formation of planar slip bands in Inconel 718 during cyclic deformation. *Scr. Mater.* 52, 603–607.
- Zhou, C., Lee, J.W., Lee, M.G., Wagoner, R.H., 2015. Implementation and application of a temperature-dependent Chaboche model. *Int. J. Plast.* 1–20.